Lab on a Chip

PAPER

View Article Online
View Journal

Cite this: DOI: 10.1039/c6lc00169f

The physical origins of transit time measurements for rapid, single cell mechanotyping†

Kendra D. Nyberg,[ab] Michael B. Scott,[a] Samuel L. Bruce,[a] Ajay B. Gopinath,[a] Dimitri Bikos,[c] Thomas G. Mason,[cd] Jin Woong Kim,[ef] Hong Sung Choi[g] and Amy C. Rowat*[ab]

The mechanical phenotype or 'mechanotype' of cells is emerging as a potential biomarker for cell types ranging from pluripotent stem cells to cancer cells. Using a microfluidic device, cell mechanotype can be rapidly analyzed by measuring the time required for cells to deform as they flow through constricted channels. While cells typically exhibit deformation timescales, or transit times, on the order of milliseconds to tens of seconds, transit times can span several orders of magnitude and vary from day to day within a population of single cells; this makes it challenging to characterize different cell samples based on transit time data. Here we investigate how variability in transit time measurements depends on both experimental factors and heterogeneity in physical properties across a population of single cells. We find that simultaneous transit events that occur across neighboring constrictions can alter transit time, but only significantly when more than 65% of channels in the parallel array are occluded. Variability in transit time measurements is also affected by the age of the device following plasma treatment, which could be attributed to changes in channel surface properties. We additionally investigate the role of variability in cell physical properties. Transit time depends on cell size; by binning transit time data for cells of similar diameters, we reduce measurement variability by 20%. To gain further insight into the effects of cell-to-cell differences in physical properties, we fabricate a panel of gel particles and oil droplets with tunable mechanical properties. We demonstrate that particles with homogeneous composition exhibit a marked reduction in transit time variability, suggesting that the width of transit time distributions reflects the degree of heterogeneity in subcellular structure and mechanical properties within a cell population. Our results also provide fundamental insight into the physical underpinnings of transit measurements: transit time depends strongly on particle elastic modulus, and weakly on viscosity and surface tension. Based on our findings, we present a comprehensive methodology for designing, analyzing, and reducing variability in transit time measurements; this should facilitate broader implementation of transit experiments for rapid mechanical phenotyping in basic research and clinical settings.

Received 4th February 2016,
Accepted 11th July 2016

DOI: 10.1039/c6lc00169f

www.rsc.org/loc

Introduction

Changes in cell mechanical properties are implicated in diverse physiological and disease phenomena, ranging from stem cell differentiation to malignant transformation. Cell mechanical phenotype or 'mechanotype' is thus emerging as a powerful, label-free biomarker to enhance clinical decision-making and diagnosis.[1] Quantitative measurements of mechanotype also facilitate a deeper understanding of the origins of altered cell physical properties. While methods such as micropipette aspiration,[2] atomic force microscopy (AFM),[3,4] and optical stretching[5] provide detailed insight into cytoskeletal and nuclear contributions to cell mechanotype, measurements are typically limited to 10 to 10^2 cells per hour. Fluid-based deformation cytometry techniques enable mechanotype measurements at faster rates of 10 to 10^4 cells per minute by tracking cells as they are deformed during flow through microfluidic constrictions or by inertial fluid flows.[6–11] Microfluidics also enable integration of complementary methods to assay additional physical properties of cells,

[a] Department of Integrative Biology and Physiology, University of California, Los Angeles, USA. E-mail: rowat@ucla.edu
[b] Department of Bioengineering, University of California, Los Angeles, USA
[c] Department of Chemistry and Biochemistry, University of California, Los Angeles, USA
[d] Department of Physics and Astronomy, University of California, Los Angeles, USA
[e] Department of Bionano Technology, Hanyang University, Ansan, 426-791, Republic of Korea
[f] Department of Applied Chemistry, Hanyang University, Ansan, 426-791, Republic of Korea
[g] Shinsegae International Co. Ltd, Seoul, 135-954, Republic of Korea
† Electronic supplementary information (ESI) available. See DOI: 10.1039/c6lc00169f

such as their electrical conductivity and membrane capacitance, as well as the ability to sort cells based on these physical features.[12–16]

In microfluidic transit experiments, cells are driven to pass through micron-scale constrictions at rates of 1 to 10^3 cells per second by applying a pressure gradient[17] or constant volume flow.[6] As cells flow through the constrictions, they deform through gaps that are up to ~3× smaller than their initial diameter; the timescale for a single cell to transit through a constriction provides a measure of its deformability. This mechanotyping method demonstrates that highly metastatic cancer cells have shorter transit times compared to less metastatic cells[9] and leukemia cells treated with chemotherapy drugs exhibit longer transit times compared to DMSO-treated control cells.[6] While transit measurements for cell mechanotyping are relatively simple and fast, there is significant variability in transit times that typically spans two to three orders of magnitude within a population of single cells. Such marked spread in transit times, in addition to measurement variability between experiments, make it challenging to use this method to robustly compare different cell types.

The broad distributions of transit times could result from phenotypic variability across a population of isogenic cells. For example, cell size varies across a population, and larger cells tend to have longer transit times.[9,18] However, even for cells with similar size (±5%, ~1 μm), transit times range over an order of magnitude.[9,18] In addition to size, cells from the same population exhibit order-of-magnitude differences in elastic modulus and viscosity, as measured by atomic force microscopy,[4,19,20] micropipette aspiration,[21–24] and optical stretching.[5,25] While stiffer cells have longer transit times,[26] the degree to which cell-to-cell heterogeneity in mechanical properties contribute to transit time variability is not well understood. Moreover, cells are viscoelastic materials and the relative contributions of elasticity and viscosity to transit measurements remain unclear. While longer transit times are associated with stiffer cells that have higher elastic moduli,[26] the time required for cells to enter microfluidic constrictions is also well predicted by the shear thinning liquid drop model, which describes a cell as a purely viscous material;[9] this makes it challenging to obtain a deeper knowledge of cell mechanical properties from transit time data.

Experimental factors may also affect the width of transit time distributions. For example, the entry velocity of cells into micron-scale pores depends on channel surface properties[9] as well as the pressure drop across a cell.[24] The impact of surface properties is especially critical when considering cell transit through polydimethylsiloxane (PDMS) channels, which are commonly plasma treated to enable covalent bonding to glass; however, this renders channels hydrophilic up to 48 hours post treatment,[27] and the influence of channel hydrophilicity on transit time variability is not well characterized. Moreover, as multiple cells simultaneously transit through the device, channel occlusions can alter flow rates, and thus entry velocities of cells into neighboring constrictions;[18] transient lane occlusions may thus also contribute to variation in transit time both within and across experiments.

Here we investigate the role of extrinsic and intrinsic factors in transit time variability with the goal of establishing more robust measurements of cell mechanotype. Using HL-60 cells as a model system, we provide a framework to reduce transit time variability due to cell size, PDMS surface properties, and transient lane occupancies. By fabricating a panel of gel and oil particles with well-defined material properties, we investigate the extent to which the broad distribution in transit times results from mechanical heterogeneity across a population. Our study also provides valuable insight into the physical underpinnings of transit time measurements, revealing that elasticity dominates transit on these millisecond timescales.

Device design and concept

Microfluidic device design

In transit time experiments, cell deformability is determined by flowing cells through micron-scale constrictions and measuring the timescale of their transit.[6–9,18] Our microfluidic device consists of a branching network of channels that extends into an array of 16 parallel lanes, where each lane contains a series of constrictions[28] (Fig. 1A and B). Cells enter the device through the inlet and first passage through a downstream filter, which helps to remove extraneous contaminants, such as chunks of PDMS that can result from device fabrication, as well as cell aggregates that are larger than 20 μm (Fig. 1A). After passing through the bifurcating channels, the cells reach the constrictions, which have a height of 5.3 μm and width of 5.2 μm (Fig. 1A and B). To transit through these constrictions, the HL-60 cells must deform down to ~40% of their original diameter.

To drive cell suspensions through the microfluidic channels, we apply air pressure, which ensures a constant pressure drop across the microfluidic device. The magnitude of applied pressure dictates the velocity of both the fluid and particles as they flow through the device. For a particle to deform through the constriction, a minimum threshold pressure, P_T, must be applied to induce sufficient strain of the particle. When the driving pressure, $P_{driving}$, is less than P_T, the particle will occlude the constriction over the experimental timescale, which is on the order of minutes. We find that $P_{driving}$ = 28 kPa (4 psi) is an adequate driving pressure, which exceeds P_T for HL-60 cell and ensures sufficient tracking of individual cells and particles. $P_{driving}$ also dictates the frequency with which cells reach the constrictions; with $P_{driving}$ = 28 kPa and a 5.3 × 5.2 μm^2 constriction, we can achieve transit events at rates of ~10^2 cells per min for cell suspensions with a density of 2 × 10^6 cells per mL.

To determine the transit time of an individual cell, we track its projected area and measure the time required for its leading edge to enter and subsequently exit the constriction region (Fig. 1C). To ensure that each cell has a similar initial state, we measure transit time data only from the first row of

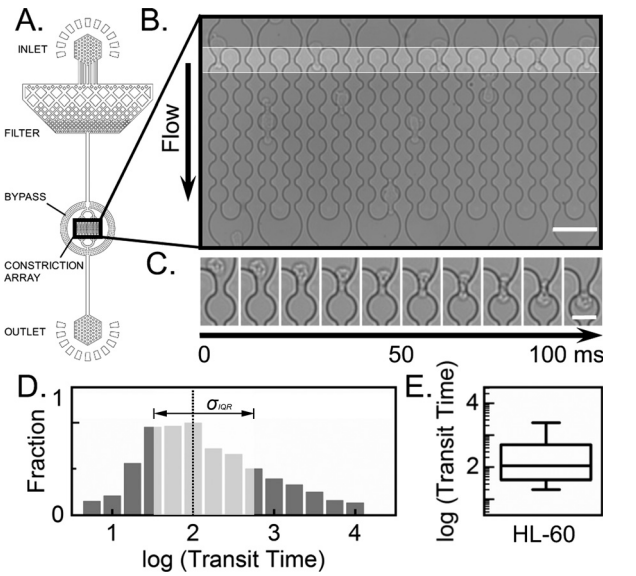

Fig. 1 Overview of microfluidic device for measuring transit time. (A) Schematic of the microfluidic device. Suspension of cells/particles enters the device through the inlet. Filters reduce the frequency of clusters of cells and larger particulates that are >20 μm from entering the constriction array. Bypass channels help to minimize fluctuations in pressure as particles transit through the device. (B) Brightfield image of the constriction array, which consists of 16 channels that each have a series of 5 μm constrictions. Transit time is defined as the time required for the leading edge of the cell to enter and exit the constriction region, which is denoted by the lighter gray region. Scale, 50 μm; (C) time series of a single cell during transit through a 5 μm constriction. The representative cell shown here has a transit time of 80 ms. Scale, 20 μm. (D) Histogram and (E) boxplot of transit times for HL-60 cells. In the histogram, light gray boxes represent the interquartile range, and dotted line represents the median. In the boxplot, the line represents the median, the box represents the interquartile range, and the whiskers represent the 10th and 90th percentiles.

constrictions; additional analyses of cell deformation and relaxation responses can be obtained from the transit through subsequent constrictions within each lane. By tracking hundreds of cells for each sample, we generate a histogram of transit times. For a single population of HL-60 cells, we observe median transit times that are on the order of tens to hundreds of milliseconds and vary over three orders of magnitude when $P_{driving}$ = 28 kPa and the constriction is 5.3 × 5.2 μm^2 (Fig. 1D). Since transit times exhibit non-normal distributions, we evaluate the width of a distribution using the bootstrapped interquartile range of the log-transformed data. As shown in Fig. 1D, the bootstrapped interquartile range and confidence interval of the log transform for HL-60 cells are σ_{IQR} = 1.1 ± 0.1.

Time and length scales of cell transit

On these tens to hundreds of millisecond timescales, we estimate that transit time measurements predominantly reflect the passive deformation response of cells as they deform through microfluidic constrictions; this passive deformation response of cells is largely determined by the organization and levels of mechanoregulating proteins, such as actin and tubulin; pharmacological perturbations of both actin and microtubules significantly alter transit times on both millisecond[18] and second[6,26,29] timescales. Over longer timescales, cells may additionally invoke active responses to mechanical loads: actomyosin contractions and transcriptional regulation can occur on the order of minutes, while protein levels are regulated on the order of minutes to hours.

Pressure drop across the constriction region

As multiple cells simultaneously transit through and occlude the bifurcated array of channels, the fluidic resistance, and thus flow rates, can fluctuate, which can impact the rate at which cells transit through constrictions. We design our microfluidic device to minimize inconsistencies in transit time that may arise from having an array of constrictions. For an array of parallel channels, the fluidic resistance is described by Kirchhoff's Law:

$$\frac{1}{R_{total}} = \frac{1}{R_{bypass}} + \frac{1}{R_{L1}} + \frac{1}{R_{L2}} + \cdots + \frac{1}{R_{LN}}. \quad (1)$$

Here, R_{total} is the total fluidic resistance along the cross-section of the channels; R_{bypass} is the fluidic resistance of the bypass channel; and R_{LN} is the fluidic resistance of N individual lanes. For a microfluidic channel with a rectangular cross-section, the relationship between the fluidic resistance, the channel height, h, and width, w, is given by the Hagen–Poiseuille relation,

$$R \propto \frac{1}{wh^3}.$$

Eqn (1) illustrates how the fluidic resistance can fluctuate as multiple cells transit through the device and transiently obstruct channels. To minimize the effect of simultaneous transit events on transit time, we design our microfluidic device to reduce fluctuations in fluidic resistance due to lane occlusions: by maximizing the number of lanes that can fit into the camera's field of view with a 20× objective, we reduce the impact of a single occlusion on the total fluidic resistance. To further buffer changes in fluidic resistance, we also include a wide bypass channel (5.3 × 300 μm^2) that surrounds the constriction region (Fig. 1A).

Based on eqn (1), we estimate that the fluidic resistance will change by <1% when a single cell transits through the array of constrictions. However, during a transit experiment, the number of occupied lanes ranges between 1 and 16 lanes; when all 16 lanes are occupied, the fluidic resistance can increase up to ~12%. To determine the effect of fluctuating lane occupancy on transit time variability and enable more robust measurements, we perform a detailed analysis of transit time as a function of lane occupancy.

Results and discussion

Transient occlusions affect transit time

With our experimental conditions of $P_{driving}$ = 28 kPa and 5.3 × 5.2 μm^2 constrictions, we find that on average 9.2 ± 2.7 out of 16 lanes are occupied during the transit of an individual HL-60 cell (Fig. 2A). For 1 to 10 lane occupancies, we observe no statistical difference between transit time distributions (Fig. 2B). However, when more than ten channels are occluded (>65% of total channels), there is a significant decrease in transit times (Fig. 2B). While our data shows a slight increase in transit times for 15 or 16 occlusions, this near-complete occlusion of all lanes happens infrequently (<1% of all transit events), so the resultant effects on cell transit time are inconclusive.

To reduce the variability in transit time that results from transient occlusion of channels, we exclude cell transit events that occur while more than ten channels are occupied. We additionally exclude cells that transit while multiple cells occupy the same lane, since this reduces the pressure drop across a single cell. Channel obstructions can also occur in regions that are outside of the field of view that we monitor during a transit experiment, such as in the filter and bypass regions. However, inspection of these regions after measurement acquisition reveals a sparse number of occluding particles or cell aggregates, which are small compared to the total cross sectional area of the filter and bypass channel. Nonetheless, to minimize any effects of unobserved occlusions, we use a new device for each video.

Age of PDMS device after plasma treatment impacts transit time

While PDMS is inherently hydrophobic, the device walls become more hydrophilic for up to 48 hours following plasma treatment,[27] which is commonly used to bond PDMS to the glass substrate. Since transit time can vary depending on the surface charge of microfluidic channels,[9] we next investigate how the age of the device following plasma treatment affects transit time. We conduct transit measurements using devices at 1, 12, 36, 48, 72 and 96 hours following plasma treatment. Compared to transit times that are obtained using a device that is aged for one hour, our results show a significant increase in transit times when measurements are performed 12 or more hours after plasma treatment. While we observe differences in the distributions of transit times at time points beyond 12 hours, there is no significant trend towards increasing or decreasing transit times. Thus, to reduce variability in transit times due to differences in device age, we conduct experiments 24 hours after plasma treatment and bonding. Consistently using 24 hour-aged devices also minimizes error that may arise from differences in the material properties of PDMS as the elastic modulus can increase by 180% following the initial cure;[30] this could impact the physical stresses on the cell during transit.

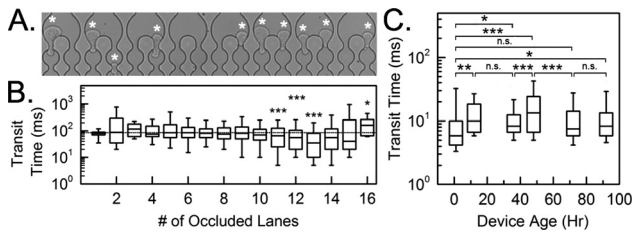

Fig. 2 Effect of extrinsic sources on transit time variability: transient lane occlusion and PDMS surface properties. (A) Brightfield image of the constriction array with 10 occupied lanes, which are denoted by the white asterisks. (B) Transit time *versus* the number of lane occlusions. Statistical significance compares the transit time distribution of each lane to the preceding lane using Mann–Whitney *U*. (C) Cell transit time as a function of the hours following plasma treatment. Statistical significance shown between the transit time distribution of each device age and the preceding time point using Mann–Whitney *U*. * for $p < 0.05$, ** for $p < 0.01$, *** for $p < 0.001$.

Transit time scales with cell size

To determine how variations in cell physical properties impact transit time measurements, we first consider the effects of cell size. The diameter of HL-60 cells ranges from 10 to 21 μm (Fig. 3A.ii), with a median of 15 μm. By tracking the projected area of cells as they transit through the constrictions, we observe that transit time increases with cell size; these observations are consistent with previous studies[9,18] (Fig. 3A.iii). To determine the scaling relation between transit time and cell size, we measure the median transit times for twelve size bins of 0.5 μm within the interquartile range of projected diameters, ranging from 19–25 μm. Performing linear regression on the log-transformed data reveals that transit time has a strong dependence on cell size (slope = 5.8 and R^2 = 0.87). By size-filtering our transit time data, we observe a 18% reduction in the variability of transit times for cells of the median size ±5% (1 μm) with a resultant σ_{IQR} = 0.9 ± 0.1 (Fig. 3A.vi).

Reduced variability for particles with uniform composition

Variability in transit time could also result from cell-to-cell differences in mechanotype. The viscous and elastic moduli of cells are largely determined by subcellular organization and structural proteins, which vary in expression level across a population of single cells. To assess particles that have uniform composition and well-defined mechanical properties,[31] we fabricate gel particles and oil droplets that have a similar size as HL-60 cells (Fig. 3B.ii and C.ii). Our panel of agarose gel particles exhibits a range of elastic moduli from 3.1 to 43 kPa (Fig. S3†); this range of elastic moduli is achieved by varying the polymer density within the droplets of a water-in-oil emulsion. We also generate oil-in-water emulsions with silicone oils that have a range of viscosities from 10^{-2} to 10^2 Pa s. In addition, we use a surfactant that enables us to regulate the surface tension of oil droplets.

Both gel particles and oil droplets deform through the constrictions of the microfluidic device using the same experimental conditions that are used for cell transit

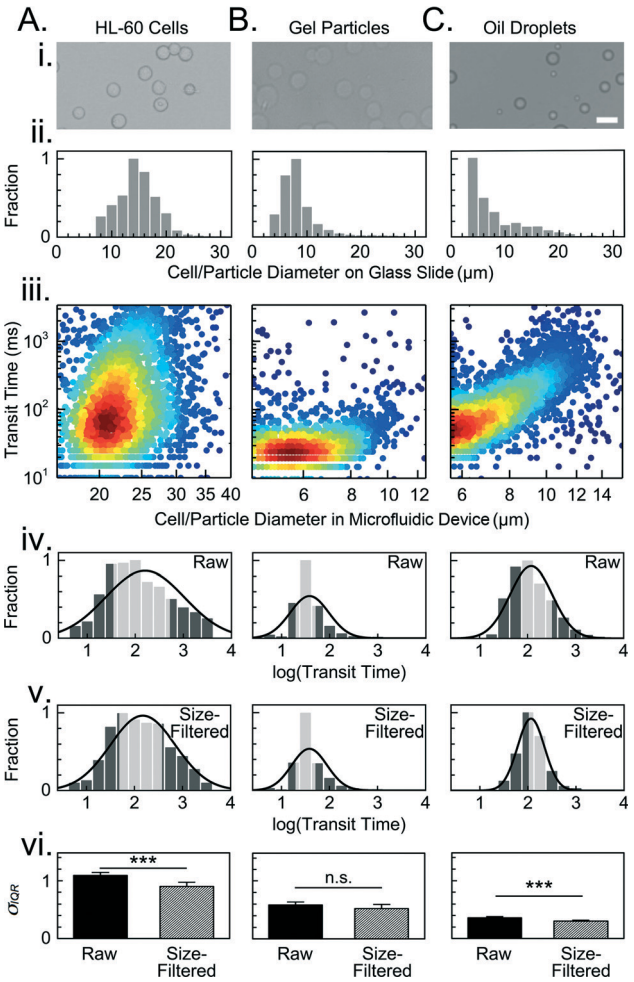

Fig. 3 Size and transit time distributions for cells and particles. (i) Brightfield images of (A) HL-60 cells, (B) representative agarose gel particles (E = 8.7 kPa), and (C) representative silicone oil droplets (η = 10^2 Pa s) on a glass slide. Scale, 15 μm. (ii) Histograms of cell/particle sizes on a glass slide. (iii) Density scatter plots of transit time *versus* cell/particle diameter as determined during flow through the microfluidic device. Color represents density of data points. Cells appear larger when they are compressed in the 5.2 μm-high channels of the microfluidic device; the gel and oil particles appear smaller in the microfluidic device as the larger particles are trapped in the filter upstream from the constriction region. (iv) Transit time distributions for (A) HL-60 cells, (B) representative agarose gel particles (E = 8.7 kPa), and (C) representative silicone oil droplets (η = 10^2 Pa s). (v) Size-filtered transit time distributions for cells and particles with diameters of the median value ±5%. For cells, the median diameter is 22 μm and for gel and oil particles, the median diameter is 7 μm. The black line overlaying the histogram represents the fitted log-normal distribution. The gray bars represent the interquartile ranges. (vi) Average bootstrapped log-transformed interquartile ranges, σ_{IQR}, for transit time distributions across the panels of E and η of the raw data (solid bar) and the size-filtered data (striped bar). Error bars represent the bootstrapped confidence intervals. Statistical significance is determined using the t-test. *** for $p < 0.001$.

measurements. As the particles flow through the constrictions, we track their size and transit time. While we observe a modest size dependence for the oil droplets, we observe no significant size dependence for our gel particles (Fig. 3B.iii and C.iii). To reduce any scaling bias and consistently compare the width of transit time distributions for cells, oil droplets, and gel particles, we filter data for all cells/particles based on the median particle size (7 ± 1 μm). Across our panel of particles within our median size filter, gel particles exhibit an average σ_{IQR} = 0.5 ± 0.2 (Fig. 3B.vi); oil droplets have an average σ_{IQR} = 0.3 ± 0.0 (Fig. 3C.vi). The reduction of σ_{IQR} for oil droplets compared to gel particles may be attributed to the uniform molecular composition of the silicone oils; by contrast, spatial heterogeneities within the agarose particles could result from variations in the fabrication process; variability in the elastic moduli of agarose gel microspheres is observed by atomic force microscopy where the standard deviation can vary up to 10%.[31] Compared to both gel and oil particles, HL-60 cells have a significantly higher σ_{IQR} = 0.9 ± 0.1 (Fig. 3A.vi); this is consistent with our hypothesis that heterogeneity in the structure and/or mechanotype of single cells is a major contributor to transit time variability.

Transit time scales with elastic modulus

Our investigation of transit times for gel and oil particles with well-defined mechanical properties also provides deeper insight into the physical underpinnings of cell transit time measurements. We first investigate how elastic modulus affects transit time using our panel of agarose gel particles, which have a similar stiffness as cells such as leukocytes and ovarian cancer cells with E = 0.1 to 1.0 kPa.[4,19] As shown in Fig. 5A, our size-filtered data across our panel of gel particles from E = 3.1 to 43 kPa reveals that stiffer particles have longer transit times than softer particles. At a fixed driving pressure of 28 kPa, gel particles with 1.0% (w/w) agarose and E = 8.7 kPa have a bootstrapped median transit time and confidence interval of 28 ± 2.5 ms. By contrast, stiffer gel particles with 2.0% (w/w) agarose and E = 17 kPa, have a bootstrapped median transit time and confidence interval of 40 ± 5.0 ms. Across our panel of gel particles, we find that the bootstrapped median transit time scales with elastic modulus, as shown by a simple linear fit (slope = 0.29 and R^2 =

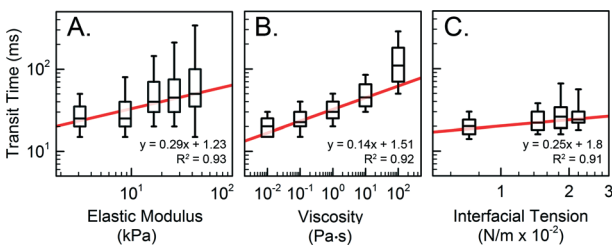

Fig. 4 Transit time depends on particle mechanical properties. Transit times for (A) agarose gel particles with increasing elastic modulus; (B) silicone oil droplets with increasing viscosity; and (C) silicone oil droplets with increasing interfacial tension. Size filtered data is shown for particles of the median diameter of 7 ± 1 μm. Boxplots show medians denoted by line, interquartile ranges represented by box, and 10th and 90th percentiles shown by whiskers. Linear regression in red displays scaling relation compared to the bootstrapped median transit times. N > 200 cells per particles for each sample.

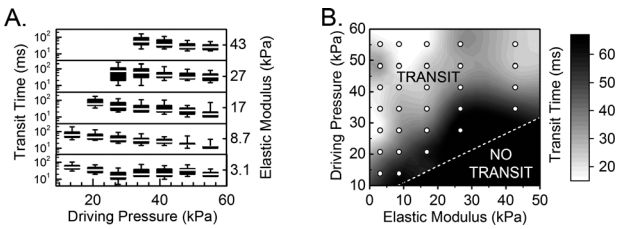

Fig. 5 Effects of driving pressure and particle elastic modulus on transit time. (A) Boxplots show transit time for agarose gel particles with well-defined elastic moduli over a range of driving pressures. Median is denoted by line, interquartile range is represented by box, and 10th and 90th percentiles are shown by whiskers. The absence of a boxplot at a given pressure reflects that no transit events occur on the experimental timescale, as $P_T < P_{driving}$. (B) Density map of transit time values as a function of driving pressure and gel particle elastic modulus. Dots represent the experimental conditions where transit time data is acquired. Dotted line represents the estimated boundary between transit and no transit regions based on measured P_T values. $N > 200$ particles for each sample.

0.93) (Fig. 4A). These results support previous findings that cells with larger elastic moduli, as extracted from optical stretching experiments, also exhibit longer transit times.[26]

Transit time weakly depends on particle viscosity

Cells are complex materials that exhibit both elastic and viscous behaviors. We next investigate how the viscosity of droplets regulates transit time by generating oil-in-water emulsions using silicone oils with well-defined viscosities from 10^{-2} to 10^{2} Pa s. We hypothesize that droplets with larger viscosities will have longer transit times, as they are comprised of larger molecules, which have longer rearrangement timescales. We select the oils to have a range of viscosities that are comparable to the viscosities of cells, which range from 10^{-2} Pa s for adherent HeLa and 3T3 cells[32] to 10^{2} Pa s for neutrophil cells.[26] To prevent coalescence and ensure that droplets remain intact during transit through the microfluidic device, we add 4% (w/w) Tween 20 surfactant. While the viscosities of our panel of oil droplets range over five orders of magnitude, we observe transit times increase by only one order of magnitude (Fig. 4B). For example, droplets with the highest viscosity of 10^{2} Pa s have a median transit time of 75 ± 2.5 ms; by contrast, droplets with the lowest viscosity of 10^{-2} Pa s have a median transit time of 20 ± 0.0 ms. Performing a linear fit to the bootstrapped median transit times of our panel of oil droplets reveals a slope of 0.14 with $R^2 = 0.92$, suggesting transit time scales with viscosity as well as elastic modulus. However, transit time scales more significantly with elastic modulus on these millisecond timescales (slope = 0.29 and $R^2 = 0.93$).

Weak dependence of interfacial tension on transit time

We next investigate the effect of interfacial tension on the transit time of oil droplets. As out-of-plane bending is required for droplets to enter the constriction, we predict that droplets with higher interfacial tensions will have longer transit times. Surface tension is analogous to the cortical tension of cells, which is largely regulated by actin and hinders out-of-plane bending of the plasma membrane.[33,34] To determine the effects of surface tension on transit time, we modify the concentration of Tween 20 surfactant in our silicone oil droplets from 0.005 to 0.1% (w/w); this results in interfacial tensions ranging from 0.7 to 2.2 × 10^{-2} N m^{-1}, as confirmed by the pendant drop technique[35] (Fig. S4†). Our experimental range of interfacial tensions is set by the critical micelle concentration (CMC) of the surfactant, which is 0.007% (w/w) at room temperature.[36] We observe that transit time tends to increase with increasing interfacial tension. For oil droplets with the highest surface tension of 2.2 × 10^{-2} N m^{-1}, the median transit time is 25 ± 3.0 ms, whereas oil droplets with a surface tension of 0.7 × 10^{-2} N m^{-1} exhibit a median transit time of 20 ± 0.0 ms. Yet even with interfacial tensions that are approximately two orders of magnitude larger than cells, our statistical analyses reveal that there is a marginal effect of interfacial tension on transit time (slope = 0.25 and $R^2 = 0.91$) compared to the effects of elastic modulus and viscosity (Fig. 4C).

Taken together, our micron-scale characterization particles reveal that elastic modulus dominates transit time when cells/particles undergo 40% strain over 0.01 to 1 second, whereas viscosity and interfacial tension have a weaker effect on these time and length scales.

Transit time depends on both particle stiffness and driving pressure

To be useful for biological and clinical applications, cell mechanotyping should have both dynamic range and sensitivity for detecting small and large differences in cell mechanical properties. To further develop a comprehensive framework for transit time experiments, we next investigate how $P_{driving}$ determines the range of mechanotypes that can effectively be measured. As transit time exhibits the strongest dependence on elastic modulus, we map transit times across our panel of gel particles and generate a phase diagram that illustrates the dynamic range for particles.

Determining the range of $P_{driving}$ that enables transit events for a range of particles with different elastic moduli is an optimization problem that involves both measurement throughput and sensitivity. To achieve rapid measurements, higher $P_{driving}$, and thus flow rates, are required. However, a single cell must be tracked for at least two frames to capture its entry and exit as well as its initial size (Fig. S5†); this can be achieved by acquiring images with high frame rates and fast exposure times. Using our CMOS fast camera, a minimum exposure time of 0.2 ms is required to reduce object blurring and delineate the location and size of a single cell (Fig. S6†); this enables us to achieve frame rates of up to 5000 frames per second. While higher image acquisition rates could be achieved with a faster camera, increased $P_{driving}$ could ultimately result in strain of PDMS channels, since $E_{PDMS} \sim 10$ MPa. The lower pressure bound must be exceeded for a transit event to occur and is set by the threshold pressure, P_T. To quantify the lower pressure bound for

particles of a given elastic modulus and size, we analyze the transit of particles with differing elastic moduli over a range of applied pressures.

We observe that stiffer particles require larger pressures to transit through the constrictions (Fig. 5). For example, we do not observe any transit events on the experimental timescale for the stiffest particles of E = 43 kPa at $P_{driving} \leq 28$ kPa. By contrast, a significant proportion of softer particles with E = 3.1 kPa transit through the constrictions at $P_{driving}$ = 28 kPa. These results highlight how $P_{driving}$ needs to be tuned to optimize the dynamic range for a set of samples with given mechanotypes. For example, to measure transit times for the softest and stiffest gel particles (E = 3.1 and 43 kPa), $P_{driving}$ should be between 34 to 55 kPa: below this pressure, stiffer particles do not transit; yet with higher pressures, softer particles transit too quickly to resolve their entry into and exit from the constriction region. Taken together, our mapping of transit times across driving pressures and particle elastic modulus results in a phase diagram, which illustrates regions where transit and no transit occur for particles of varying stiffness as a function of $P_{driving}$.

Additional sources of transit time variability

In contrast to our gel and oil particles that have relatively uniform structure and composition, cells are spatially heterogeneous materials. For example, the nucleus can occupy a significant volume within the cell and can be up to five times stiffer than the surrounding cytoplasm.[37,38] Our previous study demonstrates how the nucleus can rate-limit the deformation of cells through micron-scale gaps.[8] The nucleus can also vary in size and morphology across a population of single cells.[39] Additional geometric differences among cells could contribute to transit time variability, such as heterogeneity in the distribution of actin due to polarization and/or the position of the nucleus in a transiting cell. Moreover, cells at different stages in the cell cycle have markedly different subcellular architecture and mechanotype;[40] this likely also contributes to the variability in transit times we observe in populations of cells.

Deformation time and length scales

The deformation response of viscoelastic materials ranging from hydrogels to cells is sensitive to the time and length scales of the applied stress. Our results using calibration particles demonstrate that transit time measurements on millisecond timescales are dominated by elastic modulus. These results are consistent with our rheology data for agarose slabs, which determine the relative elastic and viscous contributions to deformations of agarose gels. By measuring the storage (G') and loss (G'') moduli across a frequency range of 0.01 to 1 Hz, we observe that G' is ~350% greater than G'' and remains relatively constant over this linear regime (Fig. S3†).

Reconstituted actin[41] and intermediate filament[42] networks also exhibit a storage modulus, G', that is typically 10 to 100 times larger than the loss modulus, G'', when probed at strain rates of 0.1 to 10 Hz. In addition, the deformation behavior of cells on similar 0.01 to 1 second timescales is largely determined by their elastic properties.[43–45] However, at higher strain rates above 1000 Hz, G'', dominates the deformation behavior, reflecting increased viscous contributions as the deformation timescale approaches the timescale for intracellular macromolecules and water molecules to rearrange.[46] For higher throughput fluid-based deformability measurements, which occur on microsecond timescales,[10] cell deformation behavior may thus depend more strongly on cell viscous properties.

The mechanical response of cells also depends on the length scale of deformation as cells are spatially heterogeneous structures. For example, the cortical region of the cell can determine the mechanical response to nanometer-scale indentations by AFM and micron-scale, out-of-plane bending induced by micropipette aspiration.[23,47] While out-of-plane bending is a requisite for cell entry into the constricted channel, cell transit events require much larger deformations of the whole cell, which involve shear and compression; these considerations support our findings that transit time exhibits the strongest dependence on elastic modulus. An elastic sphere or shell model can also recapitulate the deformations of cells and agarose beads that are induced by shear stresses during flow through microfluidic channels on millisecond timescales.[48] Our results also highlight how viscosity plays a role in transit time measurements. Indeed, viscoelastic models, such as power law rheology, can successfully predict the transit behavior of cells through microfluidic constrictions.[18] Such physical models, together with particles that have tunable elastic and viscous moduli, should enable more detailed quantitative measurements of cell mechanical properties. Particles with well-defined mechanical properties also provide much-needed calibration standards in cell mechanotyping; quantitative comparisons of cell deformability across different techniques and laboratories is critical for more advanced clinical applications of mechanotyping.

Conclusion

In this study, we identify major contributors to the cell-to-cell variability of transit times with the goal of enabling precise classification of cell populations. We demonstrate how more robust transit time measurements can be achieved by reducing variability with post acquisition analysis and size binning. We also determine the extent to which the inherent heterogeneity in cell physical properties contributes to the width of transit time distributions. Our results should enable broader application of transit time measurements for rapid, single cell mechanotyping in basic research to clinical settings.

Methods

Device fabrication

Devices are fabricated using standard photolithography methods.[49] The photoresist, SU-8 3005 (MicroChem,

Westborough, MA, USA), is patterned onto a silicon wafer using standard photolithography techniques. We confirm SU-8 thickness using a Dektak 150 Surface Profilometer (Veeco, Fullerton, CA). Polydimethylsiloxane (Sylgard 184 silicone elastomer, Dow Corning, Midland, MI, USA) is mixed with crosslinker at a 1 : 10 w/w ratio, then poured onto the mold and cured at 65 °C for 2 hours. The patterned PDMS is subsequently removed from the silicon mold and bonded to #1.5-thickness coverslips after exposure to corona discharge plasma for 1 minute and baking at 80 °C for 20 minutes.

Cell culture

HL-60 cells are cultured in RPMI-1640 media with L-glutamine (Life Technologies, Carlsbad, CA, USA), 10% fetal bovine serum, and 1% Pen/Strep (Gemini BioProducts, West Sacramento, CA, USA). Cell viability is determined before and after transit experiments using trypan blue dye and a TC20 automated cell counter (Bio-Rad, Hercules, CA, USA).

Soft particle fabrication

To make silicone oil droplets, we generate oil-in-water emulsions in deionized water with Tween 20 surfactant (Sigma-Aldrich, St. Louis, MO, USA). Deionized water with silicone oil (1 : 5 v/v) and varying concentrations of Tween 20 (5 to 100 mg mL^{-1}) are vortexed for 1 minute. The emulsion is then centrifuged at 157 × g for 3 minutes to remove air bubbles and filtered through a 35 μm mesh cap (BD Biosciences, Franklin Lakes, NJ, USA). For oil droplet experiments, we maintain a concentration of 4% (w/w) Tween 20, which is significantly greater than the critical micelle concentration (CMC) of 0.01% (w/w), so that the droplet surface is saturated and surface tension is effectively minimized.

To fabricate agarose gel particles with defined elastic moduli, we make water-in-oil emulsions with agarose dissolved in the aqueous phase. The desired (w/w) percentage of ultra-low gelling temperature agarose (Sigma-Aldrich, St. Louis, MO, USA) is added to deionized water and heated in the microwave for about 30 seconds until boiling. Mineral oil with 1% w/w Span 80 and agarose solution (1 : 5 v/v) are vortexed on high for 1 minute, filtered through a 35 μm filter (BD Biosciences, Franklin Lakes, NJ, USA), and immediately placed on ice for 1 hour to promote gelation; thereafter, the suspension is filtered a second time through a 35 μm filter. The gel particles are removed from the oil phase by adding 5 mL of deionized water and centrifuging at 157 × g for 10 minutes. To isolate the aqueous suspension of gel particles, the oil phase is removed from the top of the solution by pipetting.

Rheology measurements

To confirm the elastic moduli of our agarose gel particles, we measure the linear storage (G') and loss (G'') moduli of agarose slabs using a controlled strain shear rheometer (RFS-II, 25 mm diameter parallel plate geometry, Rheometric Scientific, Inc., Piscataway, NJ, USA). The elastic properties of these agarose slabs are similar to those found for micron-scale agarose particles.[31] Agarose solutions of varying concentrations at 20 °C are loaded into the rheometer's gap set to 1 mm, gelled to 10 °C for one hour, and then brought back to 20 °C over 30 minutes prior to measurement acquisition. A vapor trap inhibits water evaporation during gelation and measurement acquisition. To reduce slipping between the gel and the rheometer's plates, sandpaper is adhered to these plates prior to gel casting. We perform a frequency sweep from 0.1 to 10 rad s^{-1} at 1.0% strain, in the linear response limit (Fig. S3†); for each agarose concentration, this measurement is repeated three times (including loading and gelling) to obtain average values and to estimate run-to-run uncertainties. To determine Young's moduli from the measured G' values, we use a Poisson ratio of 0.5.[50] Here, we estimate the elastic modulus of our agarose gels as the Young's modulus evaluated at 1.0% strain and 1 rad s^{-1}.

Microfluidic experiments

For cell deformation experiments, 0.1% (w/w) Pluronic F-127 (Sigma-Aldrich, St. Louis, MO, USA) is added to the cell suspension to minimize cell-surface interactions (Video S1†). We drive suspensions of cells, gels, and droplets through the microfluidic device by applying air pressure to the sample. To maintain consistent fluidic resistance, we ensure the same length of tubing is used across all experiments. For experiments with cells and gel particles, PDMS devices are used 48 hours after plasma treatment and bonding. For experiments with oil droplets, PDMS channel hydrophilicity is maintained after plasma treatment by filling channels with deionized water; transit time is measured within 1 hour after plasma treatment. Transit videos are captured at 200 frames per s with a high-speed camera (MiroEx4, Vision Research, Wayne, NJ, USA) mounted on an inverted light microscope (Zeiss Observer, Zeiss, Oberkochen, Germany) with a 20×/0.40NA objective (LD Achroplan, Zeiss, Oberkochen, Germany).

Transit time analysis

Videos from microfluidic experiments are processed using a custom code in MATLAB (Mathworks, Torrance, CA, USA) (Fig. S5†). In brief, the code detects particles, tracks their location, records their size, and determines the time for the leading edge of particles to transit through the constriction region (Fig. 1C). Expanding on previously described tracking algorithms,[28] we apply here a rigorous protocol for cell detection and tracking: to determine the spatial bounds of the device constriction region, we perform an automated fit of a mask to remove regions outside of the microfluidic constrictions; to locate individual particles, we apply a set of filters, which include thresholding, dilation, erosion, median smoothing, and closing; to determine the start and end of transit, we measure the time required for the front of a particle to enter and exit the constriction region. Statistical analysis is performed using OriginPro software (OriginLab Corporation, Northampton, MA, USA). For all samples, we exclude particles with diameters smaller than 5 μm to ensure all

measured particles are sufficiently deformed as they flow through the constrictions. After these filtering procedures, we obtain 90 ± 30 cell transit measurements per minute. To determine how transit time depends on mechanical properties, we calculate the bootstrapped median transit time for each condition using 1000 random samples and apply linear regression on the log–log data. To distinguish statistically significant differences across cell treatment populations, we employ the Mann–Whitney *U* test, which enables us to compare the non-normal distributions of transit times.

Acknowledgements

We are grateful to the National Science Foundation (CAREER DBI-1254185) and the Farber Family Foundation for financial support. We also thank the Integrated Systems Nanofabrication Cleanroom at the California NanoSystems Institute and its staff for providing fabrication facilities. Thanks to Don and Ada Olins for the gift of the HL-60 cells and Angelyn Nguyen for critical reading of this manuscript and the pancreatic ductal epithelial (HPDE) cells.

References

1 H. T. K. Tse, D. R. Gossett, Y. S. Moon, M. Masaeli, M. Sohsman, Y. Ying, K. Mislick, R. P. Adams, J. Rao and D. Di Carlo, *Sci. Transl. Med.*, 2013, **5**, 212ra163.
2 M. A. Tsai, R. S. Frank and R. E. Waugh, *Biophys. J.*, 1994, **66**, 2166.
3 S. E. Cross, Y.-S. Jin, J. Rao and J. K. Gimzewski, *Nat. Nanotechnol.*, 2007, **2**, 780–783.
4 W. Xu, R. Mezencev, B. Kim, L. Wang, J. McDonald and T. Sulchek, *PLoS One*, 2012, **7**, e46609.
5 J. Guck, S. Schinkinger, B. Lincoln, F. Wottawah, S. Ebert, M. Romeyke, D. Lenz, H. M. Erickson, R. Ananthakrishnan, D. Mitchell, J. Käs, S. Ulvick and C. Bilby, *Biophys. J.*, 2005, **88**, 3689–3698.
6 M. J. Rosenbluth, W. A. Lam and D. A. Fletcher, *Lab Chip*, 2008, **8**, 1062–1070.
7 H. W. Hou, Q. S. Li, G. Y. H. Lee, A. P. Kumar, C. N. Ong and C. T. Lim, *Biomed. Microdevices*, 2009, **11**, 557–564.
8 A. C. Rowat, D. E. Jaalouk, M. Zwerger, W. L. Ung, I. A. Eydelnant, D. E. Olins, A. L. Olins, H. Herrmann, D. A. Weitz and J. Lammerding, *J. Biol. Chem.*, 2013, **288**, 8610–8618.
9 S. Byun, S. Son, D. Amodei, N. Cermak, J. Shaw, J. Ho, V. C. Hecht, M. M. Winslow, T. Jacks, P. Mallick and S. R. Manalis, *Proc. Natl. Acad. Sci. U. S. A.*, 2013, **110**, 7580–7585.
10 D. R. Gossett, H. T. K. Tse, S. A. Lee, Y. Ying, A. G. Lindgren, O. O. Yang, J. Rao, A. T. Clark, D. Di Carlo and T. K. Henry, *Proc. Natl. Acad. Sci. U. S. A.*, 2012, **109**, 7630–7635.
11 O. Otto, P. Rosendahl, A. Mietke, S. Golfier, C. Herold, D. Klaue, S. Girardo, S. Pagliara, A. Ekpenyong, A. Jacobi, M. Wobus, N. Töpfner, U. F. Keyser, J. Mansfeld, E. Fischer-Friedrich and J. Guck, *Nat. Methods*, 2015, **12**, 199–202.
12 C. Faigle, F. Lautenschläger, G. Whyte, P. Homewood, E. Martín-Badosa and J. Guck, *Lab Chip*, 2015, **15**, 1267–1275.
13 T. Yang, P. Paiè, G. Nava, F. Bragheri, R. M. Vazquez, P. Minzioni, M. Veglione, M. Di Tano, C. Mondello, R. Osellame and I. Cristiani, *Lab Chip*, 2015, **15**, 1262–1266.
14 R. M. Vazquez, G. Nava, M. Veglione, T. Yang, F. Bragheri, P. Minzioni, E. Bianchi, M. Di Tano, I. Chiodi, R. Osellame, C. Mondello and I. Cristiani, *Integr. Biol.*, 2015, **7**, 477–484.
15 J. Chen, Y. Zheng, Q. Tan, E. Shojaei-Baghini, Y. L. Zhang, J. Li, P. Prasad, L. You, X. Y. Wu and Y. Sun, *Lab Chip*, 2011, **11**, 3174–3181.
16 Y. Zhao, X. T. Zhao, D. Y. Chen, Y. N. Luo, M. Jiang, C. Wei, R. Long, W. T. Yue, J. B. Wang and J. Chen, *Biosens. Bioelectron.*, 2014, **57**, 245–253.
17 Z. Jia, L. Barbier, H. Stuart, M. Amraei, S. Pelech, J. W. Dennis, P. Metalnikov, P. O'Donnell and I. R. Nabi, *J. Biol. Chem.*, 2005, **280**, 30564–30573.
18 J. R. Lange, J. Steinwachs, T. Kolb, L. A. Lautscham, I. Harder, G. Whyte and B. Fabry, *Biophys. J.*, 2015, **109**, 26–34.
19 M. J. Rosenbluth, W. A. Lam and D. A. Fletcher, *Biophys. J.*, 2006, **90**, 2994–3003.
20 P. Cai, Y. Mizutani, M. Tsuchiya, J. M. Maloney, B. Fabry, K. J. Van Vliet and T. Okajima, *Biophys. J.*, 2013, **105**, 1093–1102.
21 E. H. Zhou, S. T. Quek and C. T. Lim, *Biomech. Model. Mechanobiol.*, 2010, **9**, 563–572.
22 M. A. Tsai, R. S. Frank and R. E. Waugh, *Biophys. J.*, 1993, **65**, 2078–2088.
23 E. Evans and A. Yeung, *Biophys. J.*, 1989, **56**, 151.
24 D. Needham and R. M. Hochmuth, *J. Biomech. Eng.*, 1990, **112**, 269–276.
25 J. M. Maloney, D. Nikova, F. Lautenschläger, E. Clarke, R. Langer, J. Guck and K. J. Van Vliet, *Biophys. J.*, 2010, **99**, 2479–2487.
26 A. E. Ekpenyong, G. Whyte, K. Chalut, S. Pagliara, F. Lautenschläger, C. Fiddler, S. Paschke, U. F. Keyser, E. R. Chilvers and J. Guck, *PLoS One*, 2012, **7**, e45237.
27 M. Morra, E. Occhiello, R. Marola, F. Garbassi, P. Humphrey and D. Johnson, *J. Colloid Interface Sci.*, 1990, **137**, 11–24.
28 D. J. Hoelzle, B. A. Varghese, C. K. Chan and A. C. Rowat, *J. Visualized Exp.*, 2014, e51474.
29 S. Gabriele, A. M. Benoliel, P. Bongrand and O. Théodoly, *Biophys. J.*, 2009, **96**, 4308–4318.
30 D. T. Eddington, W. C. Crone and D. J. Beebe, in *7th International Conference on Miniaturized Chemical and Biochemical Analysis Systems*, 2003, pp. 1089–1092.
31 A. Kumachev, E. Tumarkin, G. C. Walker and E. Kumacheva, *Soft Matter*, 2013, **9**, 2959.
32 T. Kalwarczyk, N. Ziębacz, A. Bielejewska, E. Zaboklicka, K. Koynov, J. Szymański, A. Wilk, A. Patkowski, J. Gapiński, H. J. Butt and R. Hołyst, *Nano Lett.*, 2011, **11**, 2157–2163.
33 A. C. Rowat, J. Lammerding and J. H. Ipsen, *Biophys. J.*, 2006, **91**, 4649–4664.
34 J. R. Henriksen and J. H. Ipsen, *Eur. Phys. J. E*, 2004, **14**, 149–167.
35 F. K. Hanse and G. Rodsrud, *J. Colloid Interface Sci.*, 1991, **141**, 1–9.
36 A. Patist, S. S. Bhagwat, K. W. Penfield, P. Aikens and D. O. Shah, *J. Surfactants Deterg.*, 2000, **3**, 53–58.

37 A. C. Rowat, J. Lammerding, H. Herrmann and U. Aebi, *BioEssays*, 2008, **30**, 226–236.
38 F. Guilak, J. R. Tedrow and R. Burgkart, *Biochem. Biophys. Res. Commun.*, 2000, **269**, 781–786.
39 M. Webster, K. L. Witkin and O. Cohen-Fix, *J. Cell Sci.*, 2009, **122**, 1477–1486.
40 M. A. Tsai, R. E. Waugh and P. C. Keng, *Biophys. J.*, 1996, **70**, 2023–2029.
41 O. Lieleg, K. M. Schmoller, M. Claessens and A. R. Bausch, *Biophys. J.*, 2009, **96**, 4725–4732.
42 Y.-C. Lin, N. Y. Yao, C. P. Broedersz, H. Herrmann, F. C. MacKintosh and D. A. Weitz, *Phys. Rev. Lett.*, 2010, **104**, 58101.
43 L. Deng, X. Trepat, J. P. Butler, E. Millet, K. G. Morgan, D. A. Weitz and J. J. Fredberg, *Nat. Mater.*, 2006, **5**, 636–640.
44 B. D. Hoffman, G. Massiera, K. M. Van Citters and J. C. Crocker, *Proc. Natl. Acad. Sci. U. S. A.*, 2006, **103**, 10259–10264.
45 K. E. Kasza, A. C. Rowat, J. Liu, T. E. Angelini, C. P. Brangwynne, G. H. Koenderink and D. A. Weitz, *Curr. Opin. Cell Biol.*, 2007, **19**, 101–107.
46 B. Fabry, G. N. Maksym, J. P. Butler, M. Glogauer, D. Navajas and J. J. Fredberg, *Phys. Rev. Lett.*, 2001, **87**, 148102.
47 C. Rotsch and M. Radmacher, *Biophys. J.*, 2000, **78**, 520–535.
48 A. Mietke, O. Otto, S. Girardo, P. Rosendahl, A. Taubenberger, S. Golfier, E. Ulbricht, S. Aland, J. Guck and E. Fischer-Friedrich, *Biophys. J.*, 2015, **109**, 2023–2036.
49 D. C. Duffy, J. C. McDonald, O. J. Schueller and G. M. Whitesides, *Anal. Chem.*, 1998, **70**, 4974–4984.
50 V. Normand, D. L. Lootens, E. Amici, K. P. Plucknett and P. Aymard, *Biomacromolecules*, 2000, **1**, 730–738.

